bioRxiv preprint doi: https://doi.org/10.1101/420174; this version posted September 18, 2018. The copyright holder for this preprint (which was not certified by peer review) is the author/funder, who has granted bioRxiv a license to display the preprint in perpetuity. It is made available under aCC-BY-NC-ND 4.0 International license.

Cryo-EM structures reveal bilayer remodeling during Ca^{2+} activation of a TMEM16 scramblase

Maria E. Falzone[1], Jan Rheinberger[2], Byoung-Cheol Lee[2], Thasin Peyear[3], Linda Sasset[4], Ashleigh Raczkowski[5], Edward Eng[5], Annarita Di Lorenzo[4], Olaf S. Andersen[3], Crina M. Nimigean[1,2,3], Alessio Accardi[1,2,3*]

1 Department of Biochemistry, 2 Department of Anesthesiology, 3 Department of Physiology and Biophysics, 4 Department of Pathology, Weill Cornell Medical College, 1300 York Avenue, New York, NY 10065; 5 Simons Electron Microscopy Center, New York Structural Biology Center, New York, USA,

* to whom correspondence should be addressed: ala2022@med.cornell.edu

bioRxiv preprint doi: https://doi.org/10.1101/420174; this version posted September 18, 2018. The copyright holder for this preprint (which was not certified by peer review) is the author/funder, who has granted bioRxiv a license to display the preprint in perpetuity. It is made available under aCC-BY-NC-ND 4.0 International license.

Abstract

The plasma membranes of eukaryotic cells are organized in an asymmetric manner for normal cellular function. At rest, polar and charged lipids are sequestered to the inner leaflet by the activity of ATP-driven pumps. Activation of a specialized class of membrane proteins – phospholipid scramblases – causes rapid collapse of this asymmetry and externalization of negatively charged phosphatidylserine molecules. As a result, extracellular signaling networks, controlling processes such as apoptosis, blood coagulation, membrane fusion and repair, are activated [1,2]. The TMEM16 family of membrane proteins includes phospholipid scramblases and Cl^- channels [3], all of which are Ca^{2+}-dependent. Prior structural and functional analyses of the fungal TMEM16 scramblase from *Nectria haematococca* identified a membrane-exposed hydrophilic groove that serves as the lipid translocation pathway [4-8]. In the TMEM16A channel, this pathway is sealed from the membrane, thus preventing lipid access and enabling ion permeation [9,10]. However, the mechanisms underlying Ca^{2+}-dependent gating of TMEM16 scramblases, and their effects on the surrounding lipid bilayer, remain poorly understood. Here we describe three high-resolution cryo-electron microscopy structures of a fungal scramblase from *Aspergillus fumigatus*, afTMEM16, reconstituted in lipid nanodiscs. Differences between the Ca^{2+}-free and Ca^{2+}-bound states reveal that Ca^{2+} binding induces a global rearrangement of the transmembrane and cytosolic regions, which causes the lipid pathway to open. Further, comparison of these structures and a third in the presence of a long-chain inhibitory lipid, together with functional experiments, reveal that scramblases cause profound remodeling of the surrounding membrane. Specifically, scramblase activation causes the bilayer to thin at the open lipid pathway and the outer leaflet to bend towards the center of the bilayer at the dimer interface. We propose a model in which trans-bilayer lipid movement is enabled by these membrane and protein rearrangements and provide a general mechanistic framework for phospholipid scrambling.

bioRxiv preprint doi: https://doi.org/10.1101/420174; this version posted September 18, 2018. The copyright holder for this preprint (which was not certified by peer review) is the author/funder, who has granted bioRxiv a license to display the preprint in perpetuity. It is made available under aCC-BY-NC-ND 4.0 International license.

Phospholipid scramblases are unusual membrane proteins in the sense that their environment serves as their substrate. The physiological activation of scramblases results in the fast and passive transbilayer movement of lipids. Thus, scramblase should remodel the membrane to create a conduit between leaflets though which lipids can diffuse. Current models of lipid translocation, based on the *Nectria haematococca* TMEM16 (nhTMEM16) scramblase structure, postulate a mechanism in which lipid headgroups move through a hydrophilic pathway while the tails remain embedded in the membrane core [1,4]. However, little is known about how scramblases affect the membrane structure or how Ca^{2+} binding activates TMEM16 scramblases. Here we use cryo-electron microscopy (cryo-EM) and functional experiments to address these questions. We determine the structures of the afTMEM16 scramblase reconstituted in lipid nanodiscs in an inactive (Ca^{2+}-free) and an active (Ca^{2+}-bound) conformation to resolutions of 3.9 Å and 4.0 Å respectively. These structures allow us to define key conformational rearrangements that underlie Ca^{2+}-dependent scramblase activation. Additionally, we show that scrambling is inhibited by the lipid ceramide 24:0 (C24:0) and determine the 3.6 Å resolution structure of the Ca^{2+}-bound afTMEM16/C24:0-nanodisc complex. Together, the three structures show how the scramblase interacts with its surrounding membrane substrate in different functional states.

In the presence and absence of Ca^{2+}, nanodisc-incorporated afTMEM16 adopts the TMEM16 fold (Fig. 1a,b, Extended Data Fig. 1-4), where each monomer in the dimeric protein comprises a cytosolic domain organized into a 6 α-helix (α1-α6)/3 β-strand (β1-β3) ferredoxin fold and a transmembrane region encompassing 10 α-helices (TM1-TM10) (Fig. 1c) [4,9,10]. The two monomers are related by a 2-fold axis of symmetry at the dimer interface, formed by TM10 and the cytosolic domain (Fig. 1d, Extended Data Fig. 2c). Five helices (TM1, TM2 and TM10 from one monomer and TM3, TM5 from the other) delimit the large and hydrophobic dimer cavity (Fig. 1d), where lipids are visible in the Ca^{2+}-free structure (Extended Data Fig. 4a-b). In both maps the C-terminal portion of TM6 and the linker connecting it to the short cytosolic α4 helix are not well-resolved, likely reflecting their mobility within the membrane. When processing the data without imposing symmetry between subunits, the two monomers differ in the well-resolved density of the ~22 C-terminal residues of TM6 (Extended Data Fig. 2d), likely reflecting the asymmetric orientation of the protein within the nanodisc (Extended Data Fig. 2c). The maps generated by signal subtracting the nanodisc and imposing C2 symmetry are of higher resolution and nearly

bioRxiv preprint doi: https://doi.org/10.1101/420174; this version posted September 18, 2018. The copyright holder for this preprint (which was not certified by peer review) is the author/funder, who has granted bioRxiv a license to display the preprint in perpetuity. It is made available under aCC-BY-NC-ND 4.0 International license.

identical to the non-symmetrized (C1) maps, apart from the resolved portions of TM6 (Extended Data Fig. 2e), and were therefore used for model building.

In the presence of the functionally saturating concentration of 0.5 mM Ca^{2+}, afTMEM16 adopts a conformation similar to that of Ca^{2+}-bound nhTMEM16 in detergent [4], with an overall rmsd ~1.8 Å (Extended Data Fig. 5a). The TM3-6 from each monomer form a peripheral hydrophilic cavity that opens to the membrane with a minimum diameter of ~5 Å. This pathway allows entry and translocation of phospholipid headgroups (Fig. 1d) [4-7,11,12] and is analogous to the ion pathway in the TMEM16A channel [9,10,13-15]. We identified two Ca^{2+} from the density of the cryo-EM map and of an 'omit' difference map, calculated between experimental data and simulated maps not containing Ca^{2+} (Fig. 2d). The bound Ca^{2+} ions are coordinated by five conserved acidic residues (E445 on TM6, D511 and E514 on TM7, and E534 and D547 on TM8), three polar residues (Q438, Q518, N539), and the unpaired main chain carbonyl of G441 (Fig. 2d, Extended Data Fig. 5c,d). This coordination is similar to that seen in both the nhTMEM16 scramblase and the TMEM16A channel, consistent with the evolutionary conservation of the Ca^{2+} binding residues (Extended Data Fig. 5c) [4,9,10,15-19].

To understand the changes that occur upon Ca^{2+} activation, we compared our Ca^{2+}-free and Ca^{2+}-bound structures of afTMEM16 and identified global conformational rearrangements of the Ca^{2+} binding site, lipid pathway, and cytosolic domains (Fig. 2). This contrasts with the TMEM16A channel, in which only the pathway-lining TM6 moves (Extended Data Fig. 5g) [10]. The cytosolic domains of afTMEM16 are translated ~3 Å parallel to the plane of the membrane, toward the axis of symmetry, such that the overall cytosolic domain becomes more compact and the cytosolic α7 helices tilt away from the axis of symmetry (Fig. 2a, b, Extended Data Fig. 5b). In the absence of Ca^{2+}, the afTMEM16 lipid pathway is closed to the membrane by a pinching motion of the extracellular portions of TM4 and TM6, which move toward each other by ~7 and ~3 Å, respectively (Fig. 2c). This leads to tighter packing of side chains from TM4 and TM6 and results in exposure of a hydrophobic surface to the membrane core (Fig. 2f). The narrowest access point of the lipid pathway constricts from ~5 to ~1 Å preventing lipid entry (Fig. 2g-h, Extended Data Fig. 5h). The pathway is also closed to ion entry by multiple stacked aromatic and hydrophobic side chains from TM3-7 (Extended Data Fig 5i). Residues that are important for scrambling[5,7] cluster between helices that rearrange upon Ca^{2+} binding (Extended Data Fig. 5j-k), supporting the dynamic nature of these interfaces.

bioRxiv preprint doi: https://doi.org/10.1101/420174; this version posted September 18, 2018. The copyright holder for this preprint (which was not certified by peer review) is the author/funder, who has granted bioRxiv a license to display the preprint in perpetuity. It is made available under aCC-BY-NC-ND 4.0 International license.

From the Ca^{2+}-bound conformation, TM4 bends around two prolines (P324 and P333) and TM3 slides by ~6 Å (Fig. 2c) to reach the Ca^{2+}-free conformation. Additionally, the intracellular portion of TM6 kinks around A437 by ~20º, inducing a ~20 Å vertical displacement of its terminal end (Fig. 2a,c). This displacement is similar to that seen in the TMEM16A channel, but occurs without a glycine hinge, indicating that the movement is conserved even though the sequence is not. This rearrangement displaces the three TM6 residues participating in the Ca^{2+} binding site (Q438, G441 and E445). Additional rearrangements of TM8, displacing N539 and E543, further disrupt the Ca^{2+} binding site (Fig. 2e, Extended Data Fig. 5e). No Ca^{2+} density was visible in the cryo-EM map (Extended Data Fig 5f), confirming that the scramblase is in a Ca^{2+}-free conformation. The movement of TM6 and TM8 in opposite directions partially relieves the electrostatic repulsion of the uncoordinated acidic side chains that form the Ca^{2+} binding site and opens a wide, water-accessible, conduit for ions to access the binding site from the intracellular solution.

Because these structures are of protein/nanodisc complexes, they also provide insights into the ligand-dependent interactions between the scramblase and its substrate, the surrounding membrane. The nanodisc portion of the complex is lower in resolution than the protein, preventing us from extracting information about the detailed molecular interactions between scramblase and lipids. We nevertheless observed clear remodeling of the membrane around the protein in both the 2D class averages and 3D reconstructions (Fig. 3a,b; Extended Data Fig. 6a-d). The remodeling was observed in 3 independent datasets, whose resolutions varied between ~4 and ~9 Å for the proteinaceous regions (Extended Data Fig. 6c,d), indicating the robust and reproducible nature of the observation as well as its independence from data processing algorithms. The asymmetric arrangement of the afTMEM16/nanodisc complex is less pronounced in the absence of Ca^{2+} (Fig. 3a,b, Extended Data Fig. 6e-f). This raises the possibility that the acentric disposition of the protein within the nanodisc membrane depends on the activity and conformation of the protein.

3D reconstructions of the afTMEM16/nanodisc complexes with and without Ca^{2+} show that the scramblase remodels the lipid bilayer near the translocation pathway and at the dimer cavity (Fig. 3a-c). In the presence of Ca^{2+}, the density of the nanodisc near the lipid transport pathway is less than in the rest of the complex (Fig. 3a, inset). In contrast, in the absence of Ca^{2+} the density in this region is comparable to the rest of the nanodisc (Fig. 3b, inset). This suggests that the membrane is thinner near the lipid pathway of an active scramblase, consistent with recent

bioRxiv preprint doi: https://doi.org/10.1101/420174; this version posted September 18, 2018. The copyright holder for this preprint (which was not certified by peer review) is the author/funder, who has granted bioRxiv a license to display the preprint in perpetuity. It is made available under aCC-BY-NC-ND 4.0 International license.

proposals [7,8,12]. The 3D reconstructions additionally reveal a thickening of the membrane around the long TM3 in one monomer and thinning by ~20% at the short TM1 of the other, resulting in a pronounced bending of the upper leaflet near the dimer cavities (Fig. 3c). The membrane slant matches the tilted plane defined by the extracellular ends of the five cavity-lining helices (Fig. 3c). The shortest ones (TM1 and TM2) are unusually rich in aromatic side chains (Fig. 3c), which anchor TM segments to membrane/solution interfaces [20], creating a favorable environment for both phospholipid headgroups and tails. This architecture is conserved in the nhTMEM16 scramblase (Extended Data Fig. 6h-j). However, the TMEM16A channel has longer TM1, with fewer aromatics, and a shorter TM3 (Extended Data Fig. 6i) explaining the lack of membrane remodeling upon its reconstitution in nanodiscs [9]. A quantitative analysis of the nanodisc density at the pathway and dimer cavities supports our observation that activation of afTMEM16 bends the upper leaflet near the dimer cavity and thins the membrane near the translocation pathway (Extended Data Fig. 7).

The hypothesis that afTMEM16 thins the membrane near the lipid pathway during scrambling makes two testable predictions: thicker membranes should impair scrambling and the membrane density at the pathway should be higher when scrambling is inhibited. Indeed, when membrane thickness was increased from ~38 to ~45 Å using lipids with longer acyl chains [21], the rate of scrambling, determined with a dithionite-based fluorescence assay[12,18], was reduced ~500-fold in the presence of Ca^{2+} (Fig. 3d, e Extended Data Fig. 8a-d). To identify scrambling inhibitors, we considered naturally-occurring bilayer-modifying constituents of cellular membranes. In particular, we tested ceramides because they regulate cellular processes that involve activation of phospholipid scramblases, such as blood coagulation, inflammation and apoptosis[22-26]. We found that addition of physiological levels of long chain ceramides potently inhibits scrambling by reconstituted afTMEM16 (Fig. 3f). Among the tested ceramides, Ceramide 24:0 (C24:0) inhibits scrambling ~250-fold when added at 5 mole% (Fig. 3f). The inhibitory effect depends on ceramide concentration, with minimal effects at 1 mole% and saturation, as C24:1 is nearly inert (Fig. 3f, Extended Data Fig. 14). The length of the ceramide acyl chain is also important as C22:0 is as potent as C24:0 while C18:0 has minimal effect at 5 mole% (Fig. 3f, Extended Data Fig. 8e-k). We used a gramicidin-based fluorescence quench assay [27] to investigate whether C24:0 and C24:1 differentially affect bulk membrane properties, such as thickness and fluidity. The assay monitors alterations in the gramicidin monomer↔dimer equilibrium, which varies with changes in

bioRxiv preprint doi: https://doi.org/10.1101/420174; this version posted September 18, 2018. The copyright holder for this preprint (which was not certified by peer review) is the author/funder, who has granted bioRxiv a license to display the preprint in perpetuity. It is made available under aCC-BY-NC-ND 4.0 International license.

membrane thickness and elasticity [28,29]. Addition of C24:0 or C24:1 comparably reduces gramicidin activity (Extended Data Fig. 8l-n), indicating that both ceramides stiffen and/or thicken the membrane to a similar extent. The comparable effects of C24:0 and C24:1 on membrane properties suggest that their distinct effects on afTMEM16 scrambling might reflect specific interactions with the scramblase and/or their differential ability to form gel-like microdomains in membranes [30-32].

To understand how ceramides affect scrambling, we determined the 3.6 Å resolution structure of Ca^{2+}-bound afTMEM16 in nanodiscs containing 5 mole% C24:0 (Extended Data Fig. 1, 3), a concentration that fully inhibits activity (Fig. 3f). The protein adopts a conformation where the lipid pathway is open to the membrane and both Ca^{2+}-binding sites are occupied (Extended Data Fig. 3j, 9a), and is nearly identical to the Ca^{2+}-bound active state, with an overall rmsd<1 Å (Extended Data Fig. 9b). No individual lipids are resolved within the pathway, while several partial lipid chains are visible in the dimer cavity (Extended Data Fig. 4c). Interestingly, although the protein adopts an active conformation, the surrounding membrane more closely resembles that of the Ca^{2+}-free than the Ca^{2+}-bound complex: the upper leaflet is less bent at the dimer cavity and the density near the pathway is comparable to that of the rest of the nanodisc (Extended Data Fig. 6g, 9c-d). Indeed, in this complex the relative densities of the lipid pathway and dimer interfaces are similar to those seen in the Ca^{2+}-free complex (Extended Data Fig. 7). Thus, ceramide-mediated inhibition of scrambling reduces nanodisc remodeling, even though afTMEM16 is in an open conformation. These results are consistent with the idea that phospholipid scrambling entails a thinning of the membrane near the lipid transport pathway. Finally, our findings show that while the conformation of the lipid translocation pathway is controlled by Ca^{2+} binding, the physico-chemical properties of the membrane determine whether lipid scrambling actually occurs.

Our structural and functional experiments provide detailed insights into the activation mechanism of TMEM16 phospholipid scramblases (Fig. 1, 2) and how these proteins remodel the surrounding membrane to facilitate the transfer of lipids between leaflets (Fig. 3). The Ca^{2+}-free and Ca^{2+}-bound structures of afTMEM16 define the extremes of the Ca^{2+}-dependent activation process and suggest that opening of the lipid pathway is controlled by two structural elements, TM4 and TM6 (Fig. 1, 2). Without Ca^{2+}, TM4 and TM6 are bent, sealing the pathway from the lipid membrane (Fig. 4a). The first step in activation is presumably Ca^{2+} binding, which facilitates the transition of TM6 to a straight conformation and its disengagement from TM4, allowing TM6

bioRxiv preprint doi: https://doi.org/10.1101/420174; this version posted September 18, 2018. The copyright holder for this preprint (which was not certified by peer review) is the author/funder, who has granted bioRxiv a license to display the preprint in perpetuity. It is made available under aCC-BY-NC-ND 4.0 International license.

to move towards TM8 and complete the formation of the Ca^{2+} binding site (Fig. 4b). The resulting conformation is similar to that of Ca^{2+}-bound TMEM16A, where TM6 is straight but lipid access is prevented by a bent TM4 [9,10]. Straightening of the TM4 helix opens the lipid pathway to enable lipid translocation, as seen in Ca^{2+}-bound afTMEM16 and nhTMEM16 (Fig. 4c)[4]. To complete the gating scheme, we propose a state where TM4 is straight and TM6 is bent (Fig. 4d), which would give rise to a partially opened lipid pathway. This conformation, while not yet observed experimentally, would account for the low, basal activity of reconstituted scramblases in the absence of Ca^{2+} (Extended Data Fig. 8) [4,7,11,12,18]. Within this gating mechanism, Ca^{2+}-activated TMEM16 channels would naturally arise from scramblases via mutations that render straightening of TM4 unfavorable, while maintaining the Ca^{2+}-dependent rearrangement of TM6 (Fig. 4a,b) [9,10]. Indeed, in the Ca^{2+}-free afTMEM16 scramblase, the pathway and cytosolic domain adopt conformations similar to those seen in the TMEM16A channel (Extended Data Fig. 10). Mutations that convert TMEM16A into a scramblase [5,6] might re-enable the TM4 transition.

Our structures of afTMEM16 scramblase/nanodisc complexes suggest that lipid scrambling is the product of two features of the TMEM16 architecture: the dimer cavities and the lipid pathway (Fig. 3). The slanted architecture of the dimer cavities induces membrane thinning on one side of the open lipid pathway and thickens it on the opposite side. This creates a membrane region that is highly curved, thin and disordered, all of which will facilitate lipid transfer between leaflets through the conduit formed by the open pathway (Fig. 4e) [33-35]. In the Ca^{2+}-free conformation of the scramblase, the closed pathway prevents lipid entry and membrane thinning (Fig. 4f). Similar mechanisms, where hydrophobic mismatches induce local distortion of membranes to lower the energy barrier for lipid movement through hydrophilic grooves, could be generally applicable to other scramblases. Moreover, the finding that native components of the plasma membrane, such as ceramides, specifically modulate the activity of afTMEM16 suggest that modulation of bilayer properties and composition might constitute secondary layers of regulatory control for the *in vivo* activation of scramblases.

bioRxiv preprint doi: https://doi.org/10.1101/420174; this version posted September 18, 2018. The copyright holder for this preprint (which was not certified by peer review) is the author/funder, who has granted bioRxiv a license to display the preprint in perpetuity. It is made available under aCC-BY-NC-ND 4.0 International license.

Methods

Protein Expression and Purification

afTMEM16 was expressed and purified as described [18]. Briefly, *S. cerevisiae* carrying pDDGFP2 [36] with afTMEM16 were grown in yeast synthetic drop-out medium supplemented with Uracil (CSM-URA; MP Biomedicals) and expression was induced with 2% (w/v) galactose at 30° for 22 hours. Cells were collected, snap frozen in liquid nitrogen, lysed by cryomilling (Retsch model MM400) in liquid nitrogen (3 × 3 min, 25 Hz), and resuspended in buffer A (150 mM KCl, 10% (w/v) glycerol, 50 mM Tris-HCl, pH8) supplemented with 1 mM EDTA, 5 µg ml^{-1} leupeptin, 2 µg ml^{-1} pepstatin, 100 µM phenylmethane sulphonylfluoride and protease inhibitor cocktail tablets (Roche). Protein was extracted using 1% (w/v) digitonin (EMD biosciences) at 4°C for 2 hours and the lysate was cleared by centrifugation at 40,000 g for 45 minutes. The supernatant was supplemented with 1 mM $MgCl_2$ and 10 mM Imidazole, loaded onto a column of Ni-NTA agarose resin (Qiagen), washed with buffer A + 30 mM Imidazole and 0.12% digitonin, and eluted with buffer A + 300 mM Imidazole and 0.12% digitonin. The elution was treated with Tobacco Etch Virus protease overnight to remove the His tag and then further purified on a Superdex 200 10/300 GL column equilibrated with buffer A supplemented with 0.12% digitonin (GE Lifesciences). The afTMEM16 protein peak was collected and concentrated using a 50 K_d molecular weight cut off concentrator (Amicon Ultra, Millipore).

Liposome reconstitution and lipid scrambling assay

Liposomes were prepared as described [18], briefly lipids in chloroform (Avanti), including 0.4% w/w tail labeled NBD-PE, were dried under N_2, washed with pentane and resuspended at 20 mg ml^{-1} in buffer B (150 mM KCl, 50 mM HEPES pH 7.4) with 35 mM 3-[(3-cholamidopropyl)dimethylammonio]-1- propanesulfonate (CHAPS). afTMEM16 was added at 5 µg protein/mg lipids and detergent was removed using four changes of 150 mg ml^{-1} Bio-Beads SM-2 (Bio-Rad) with rotation at 4°C. Calcium or EGTA were introduced using sonicate, freeze, and thaw cycles. Liposomes were extruded through a 400 nm membrane and 20 µl were added to a final volume of 2 mL of buffer B + 0.5 mM $Ca(NO_3)_2$ or 2 mM EGTA. The fluorescence intensity of the NBD (excitation-470 nm emission-530 nm) was monitored over time with mixing in a PTI spectrophotometer and after 100 s sodium dithionite was added at a final concentration of 40 mM (Fig. 3d). Data was collected using the FelixGX 4.1.0 software at a sampling rate of 3 Hz. All

bioRxiv preprint doi: https://doi.org/10.1101/420174; this version posted September 18, 2018. The copyright holder for this preprint (which was not certified by peer review) is the author/funder, who has granted bioRxiv a license to display the preprint in perpetuity. It is made available under aCC-BY-NC-ND 4.0 International license.

experiments with added ceramide lipids were carried out in the background of 1-palmitoyl-2-oleoyl-sn-glycero-3-phosphoethanolamine (POPE), 1-palmitoyl-2-oleoyl-sn-glycero-3-phospho-(1'-rac-glycerol) (POPG) at a ratio of 3:1. Ceramides tested include: N-stearoyl-D-erythro-sphingosine (C18:0), N-behenoyl-D-erythro-sphingosine (C22:0), N-lignoceroyl-D-erythro-sphinganine (C24:0), and N-nervonoyl-D-erythro-sphingosine (C24:1) all of which were tested at 1 mole% and 5 mole% (Extended Data Fig. 8). Chain length experiments were done in the background of 7PC:3PG due to the availability of the long chain lipids. Lipids used include 1-palmitoyl-2-oleoyl-glycero-3-phosphocholine (POPC, 16-18C), POPG (16-18C), 1,2-dierucoyl-sn-glycero-3-phosphocholine (DEPC, 22-22C) and 1,2-dielaidoyl-phosphatidylglycerol (DEPG, 22-22C) (Extended Data Fig, 8).

Quantification of scrambling activity

Quantification of the scrambling rate constants by afTMEM16 was determined as recently described [7,12]. Briefly, the fluorescence time course was fit to the following equation

$$F_{tot}(t) = f_0(L_i^{PF} + (1 - L_i^{PF})e^{-\gamma t}) + \frac{(1-f_0)}{D(\alpha+\beta)}\{\alpha(\lambda_2+\gamma)(\lambda_1+\alpha+\beta)e^{\lambda_1 t} + \lambda_1\beta(\lambda_2+\alpha+\beta+\gamma)e^{\lambda_2 t}\} \qquad (1)$$

Where $F_{tot}(t)$ is the total fluorescence at time t, L_i^{PF} is the fraction of NBD-labeled lipids in the inner leaflet of protein free liposomes, $\gamma=\gamma'[D]$ where γ' is the second order rate constant of dithionite reduction, [D] is the dithionite concentration, f_0 is the fraction of protein-free liposomes in the sample, α and β are respectively the forward and backward scrambling rate constants and

$$\lambda_1 = -\frac{(\alpha+\beta+\gamma)-\sqrt{(\alpha+\beta+\gamma)^2-4\alpha\gamma}}{2} \quad \lambda_2 = -\frac{(\alpha+\beta+\gamma)+\sqrt{(\alpha+\beta+\gamma)^2-4\alpha\gamma}}{2}$$

$$D = (\lambda_1+\alpha)(\lambda_2+\beta+\gamma) - \alpha\beta$$

The free parameters of the fit are f_0, α and β while L_i^{PF} and γ are experimentally determined from experiments on protein-free liposomes. In protein-free vesicles a very slow fluorescence decay is visible likely reflecting a slow leakage of dithionite into the vesicles or the spontaneous flipping of the NBD-labeled lipids. A linear fit was used to estimate the rate of this process was estimated to be $L=(5.4\pm1.6)\cdot10^{-5}\ s^{-1}$ (n>160). For WT afTMEM16 and most mutants the leak is >2 orders of magnitude smaller than the rate constant of protein-mediated scrambling and therefore is negligible. All conditions were tested side by side with a control preparation in standard conditions. In some rare cases this control sample behaved anomalously, judged by scrambling fit

bioRxiv preprint doi: https://doi.org/10.1101/420174; this version posted September 18, 2018. The copyright holder for this preprint (which was not certified by peer review) is the author/funder, who has granted bioRxiv a license to display the preprint in perpetuity. It is made available under aCC-BY-NC-ND 4.0 International license.

parameters outside 3 times the standard deviation of the mean for the WT. In these cases the whole batch of experiments was disregarded.

MSP1E3 Purification and Nanodisc Reconstitution

MSP1E3 was expressed and purified as described [37]. Briefly, MSP1E3 in a pET vector (Addgene #20064) was transformed into the BL21-Gold (DE3) strain (Stratagene). Transformed cells were grown in LB media supplemented with Kanamycin (50 mg l^{-1}) to an OD_{600} of 0.8 and expression was induced with 1 mM IPTG for 3 hrs. Cells were harvested and resuspended in buffer C (40 mM Tris-HCl pH 78.0, 300 mM NaCl) supplemented with 1% Triton X-100, 5 μg ml^{-1} leupeptin, 2 μg ml^{-1} pepstatin, 100 μM phenylmethane sulphonylfluoride and protease inhibitor cocktail tablets (Roche). Cells were lysed by sonication and the lysate was cleared by centrifugation at 30,000 g for 45 min at 4° C. The lysate was incubated with Ni-NTA agarose resin for one hour at 4 °C followed by sequential washes with: buffer C + 1% triton-100, buffer C + 50 mM sodium cholate + 20 mM imidazole and buffer C + 50 mM imidazole. The protein was eluted with buffer C + 400 mM imidazole, desalted using a PD-10 desalting column (GE life science) equilibrated with buffer D (150 mM KCl, 50 mM Tris pH 8.0) supplemented with 0.5 mM EDTA. The final protein was concentrated to ~8 mg ml^{-1} (~250 μM) using a 30 kDa molecular weight cut off concentrator (Amicon Ultra, Millipore), flash frozen and stored at -80 °C.

Reconstitution of afTMEM16 in nanodiscs was carried out as follows, 3POPE:1POPG lipids in chloroform (Avanti) were dried under N_2, washed with pentane and resuspended in buffer D and 40 mM sodium cholate (Anatrace) at a final concentration of 20 mM. Molar ratios of 1:0.8:60 MSP1E3:afTMEM16:lipids were mixed at a final lipid concentration of 7 mM and incubated at room temperature for 20 minutes. Detergent was removed via incubation with Bio-Beads SM-2 (Bio-Rad) at room temperature with agitation for two hours and then overnight with fresh Bio-Beads SM2 at a concentration of 200 mg ml^{-1}. The reconstitution mixture was purified using a Superose6 Increase 10/300 GL column (GE Lifesciences) pre-equilibrated with buffer D plus 5 mM EDTA or 0.5 mM $CaCl_2$ and the peak corresponding to afTMEM16-containing nanodiscs was collected for cryo electron microscopy analysis.

Electron Microscopy Data Collection

bioRxiv preprint doi: https://doi.org/10.1101/420174; this version posted September 18, 2018. The copyright holder for this preprint (which was not certified by peer review) is the author/funder, who has granted bioRxiv a license to display the preprint in perpetuity. It is made available under aCC-BY-NC-ND 4.0 International license.

3.5 uL of afTMEM16-containing nanodiscs (7mg mL^{-1}) supplemented with 3 mM Fos-Choline-8-Fluorinated (Anatrace) was applied to a glow-discharged UltrAuFoil R1.2/1.3 300-mesh gold grid (Quantifoil) and incubated for one minute under 100% humidity at 15°C. Following incubation, grids were blotted for 2 s and plunge frozen in liquid ethane using a Vitrobot Mark IV (FEI). For the ceramide and EDTA samples, micrographs were acquired on a Titan Krios microscope (FEI) operated at 300 kV with a K2 Summit direct electron detector (Gatan), using a slid width of 20 eV on a GIFQuantum energy filter and a Cs corrector with a calibrated pixel size of 1.0961 Å /pixel. A total dose of 62.61 $e^{-}/Å^2$ distributed over 45 frames (1.39 $e^{-}/ Å^2$/frame) was used with an exposure time of 9s (200ms/frame) and defocus range of -1.5μm to -2.5μm. For the $CaCl_2$ sample, micrographs were acquired on a Titan Krios microscope (FEI) operated at 300 kV with a K2 Summit direct electron detector with a calibrated pixel size of 1.07325 Å /pixel. A total dose of 69.97 $e^{-}/Å^2$ distributed over 50 frames (1.39 $e^{-}/ Å^2$/frame) was used with an exposure time of 10s (200ms/frame) and a defocus range of -1.5 μm to -2.5 μm. For all samples, automated data collection was carried out using Leginon [38].

Image Processing

For all data sets, motion correction was performed using MotionCorr2 [39] and contrast transfer function (CTF) estimation was performed using CTFFIND4 [40] both via Relion 2.0.3 [41]. After manually picking ~2,000 particles, the resulting 2D class-averages were used as templates for automated particle picking in Relion. The particles were extracted using a box size of 275 Å with 2xbinning and subjected to 2D classification ignoring CTFs until the first peak. For the Ca^{2+}-free and ceramide data sets, particles selected from 2D classification (245,835 from Ca^{2+}-free, and 185,451 from ceramide) were subjected to 3D classification using the nhTMEM16 crystal structure low-pass filtered to 40 Å as an initial model. For the 0.5 mM $CaCl_2$ sample two data sets were used; particles selected from the first round of 2D classification from each data set were combined and subjected to a second round of 2D classification and the resulting 302,092 particles were subjected to the same 3D classification procedure. Particles from 3D classes with defined structural features (100,268 $CaCl_2$, 70,535 Ca^{2+}-free, 90,709 ceramide,) were combined and re-extracted without binning and refined without enforcing symmetry using an initial model generated in CryoSPARC [42].

bioRxiv preprint doi: https://doi.org/10.1101/420174; this version posted September 18, 2018. The copyright holder for this preprint (which was not certified by peer review) is the author/funder, who has granted bioRxiv a license to display the preprint in perpetuity. It is made available under aCC-BY-NC-ND 4.0 International license.

Initial refinement of the afTMEM16 dataset in 0.5 mM $CaCl_2$ (referred to as "+Ca^{2+}") resulted in a map with a resolution of ~7 Å. The protein was symmetric, with the exception of the resolved portion of TM6 in each monomer (Extended Data Fig. 2d). The complex was however not two-fold symmetric due to the off-center placement of the protein within the nanodisc (Extended Data Fig. 2c). Therefore, data processing was carried out in parallel with C2 symmetry and without enforcing symmetry (in C1 symmetry). The particles from first C1 refinement were subjected to an additional round of 3D classification, using a mask that excluded the nanodisc and maintaining the particle orientations determined by the previous refinement. The best class from 3D classification with 27,948 particles was selected for further refinement and particle polishing. Masked refinement following particle polishing resulted in a 4.36 Å final map. To refine with C2 symmetry, the particles were polished and the nanodisc was removed using signal subtraction in Relion and the subtracted particles were refined using C2 symmetry, resulting in a 4.5 Å map. Using this map, a similar procedure to the C1 processing was carried out in which the best two classes from 3D classification without alignment applying a mask including the protein (37,146 particles) were selected for further refinement. Masked refinement of these classes yielded a 4.05 Å final density map. The C1 and C2 density maps were extensively compared and determined to be nearly identical except for the resolved portion of TM6 (Extended Data Fig. 2e). The C2 map was used for model building while the C1 map was used for analysis of the afTMEM16/nanodisc complex.

For the Ca^{2+}-free data set (referred to as "0 Ca^{2+}"), the first refinement resulted in a map with a resolution of ~6 Å. As with the +Ca^{2+} sample, the protein was two-fold symmetric with the exception of the resolved portion of TM6 and the overall afTMEM16/nanodisc complex was not symmetric (Extended Data Fig. 2c-d). Therefore, data was processed in parallel using both C1 and C2 symmetries as described above. The C1 map was classified and the best class from 3D classification with a mask excluding the nanodisc (38,550 particles) was selected for further refinement and particle polishing. Masked refinement following particle polishing resulted in a 4.00 Å final density map. Masked, C2 refinement following polishing and signal subtraction resulted in a 3.89 Å map. The C2 map was used for model building while the C1 map was used for analysis of the afTMEM16/nanodisc complex in 0 Ca^{2+}.

For the data set in the presence of 0.5 mM $CaCl_2$ and 5 mole% C24:0 (referred to as "+Cera"), the resulting refinement showed that the nanodisc and the protein were C2 symmetric.

bioRxiv preprint doi: https://doi.org/10.1101/420174; this version posted September 18, 2018. The copyright holder for this preprint (which was not certified by peer review) is the author/funder, who has granted bioRxiv a license to display the preprint in perpetuity. It is made available under aCC-BY-NC-ND 4.0 International license.

Therefore, further processing was completed with C2 symmetry enforced. Refinement resulted in a map with a resolution of 3.89 Å. An additional round of 3D classification was carried out using a mask excluding the nanodisc and maintaining the particle orientations determined by the previous refinement. The highest resolution class with 24,602 particles was selected for further refinement and particle polishing. Masked refinement following particle polishing resulted in a final map with a final average resolution of 3.59 Å.

The final resolution of all maps was determined by applying a soft mask around the protein and the gold-standard Fourier shell correlation (FSC) = 0.143 criterion using Relion Post Proccessing (Extended Data Fig. 1g, j, 2g, j,16g). BlocRes from the Bsoft program was used to estimate the local resolution for all final maps [43,44](Extended Data Figure 1f). The two lower resolution +Ca^{2+} datasets mentioned were processed as described above up to the first refinement step due to the limited resolution (Extended Data Fig. 6).

Model Building, Refinement, and Validation

The maps were of high quality and we built atomic models for each structure for the transmembrane domain, most of the cytosolic region and connecting loops (Extended Data Fig. 3), as well as identifying seven partial lipids in the +Cera structure and two in the Ca^{2+}-free structure (Extended Data Fig. 4). The model of afTMEM16 in the presence of ceramide was built first, due to the higher resolution of the map. The crystal structure of nhTMEM16 (PDBID 4wis) was used as a starting model and docked into the density map using chimera and the jiggle fit script in COOT [45](https://www2.mrc-lmb.cam.ac.uk/groups/murshudov/index.html), and mutated to match the afTMEM16 sequence. The final model contains residues 13-54, 60-119, 126-259, 270-312, 316-399, 418-461, 490-597, 602-657 and 705-724 and the following residues were truncated due to missing side chain density: L43, Q49, R53, K69, K70, E94, K100, Q102, K129, H130, D137, K257, E258, L316, E461, H555, F705, K713, E714, and E717. The model was improved iteratively by real space refinement in PHENIX imposing crystallographic symmetry and secondary structure restraints followed by manual inspection and removal of outliers. The model for the +Ca^{2+} structure was built using the refined +Cera structure (PDBID 6E1O) as an initial model, that was docked into the +Ca^{2+} density using the jigglefit script in COOT [45] (https://www2.mrc-lmb.cam.ac.uk/groups/murshudov/index.html), manually inspected, and refined using real space refinement in PHENIX as above [46,47]. The final model contains residues

bioRxiv preprint doi: https://doi.org/10.1101/420174; this version posted September 18, 2018. The copyright holder for this preprint (which was not certified by peer review) is the author/funder, who has granted bioRxiv a license to display the preprint in perpetuity. It is made available under aCC-BY-NC-ND 4.0 International license.

13-54, 60-119, 128-258, 270-312, 316-400, 420-460, 490-594, 602-659 and 705-724, and the following residues were truncated due to missing side chain density: D17, Q49, R53, K100, Q102, E104, K129, H130, N135, D137, E164, H247, K254, K257, H460, K550, H595, R710, K713, E714, E717, and L720. The model for the 0 Ca^{2+} structure was built using the +Cera model as a starting point and regions where the density differed were built manually (TM3, TM4 and TM6) or rigid body refined where smaller rearrangements were observed. The final model contains residues 13-54, 60-119, 128-258, 270-312, 316-400, 420-460, 490-594, 602-659 and 705-724, and the following residues were truncated due to missing side chain density: D17, F36, R53, K70, E94, K100, Q102, E132, K241, H247, R250, K257, E310, K317, K634, K642, Y654, R704, R708, E714, E717. For all three structures, the density in the regions of TM3 and TM4 and the connecting loop (residues 274-352) was less well-defined than remainder of the structure and the model may be less accurate in this area.

To validate the refinement, the FSC between the refined model and the final map was calculated (FSCsum) (Extended Data Fig. 11). To evaluate for over-fitting, random shifts of up to 0.3 Å were introduced in the final model and the modified model was refined using PHENIX against one of the two unfiltered half maps.. The FSC between this modified-refined model and the half map used in refinement (FSCwork) was determined and compared to the FSC between the modified-refined model and the other half map (FSCfree) which was not used in validation or refinement. The similarity in these curves indicates that the model was not over-fit (Extended Data Fig. 11). The quality of all three models was assessed using MolProbity [48] and EMRinger [49], both of which indicate that the models are of high quality (Extended Data Fig. 11).

Difference map calculation

To compare the maps resulting from C1 and C2 processing in the 0 Ca^{2+} and +Ca^{2+} structures, we calculated a difference map between the two volumes using the volume operation subtract function in chimera [50] (Extended Data Fig 2e). We used 'omit density' to assign the placement of several lipids in the 0 Ca^{2+} and +Cera structures and the Ca^{2+} ions in the +Ca^{2+} and +Cera structures which were calculated using the 'phenix.real_space_diff_map' function in PHENIX [9,46,47]. Briefly, completed models without the ligand in question were used to generate a theoretical density map

bioRxiv preprint doi: https://doi.org/10.1101/420174; this version posted September 18, 2018. The copyright holder for this preprint (which was not certified by peer review) is the author/funder, who has granted bioRxiv a license to display the preprint in perpetuity. It is made available under aCC-BY-NC-ND 4.0 International license.

which was subtracted from the experimental density map. In the subtracted map, areas of ligand density appeared as positive density.

Quantification of membrane remodeling

Density maps containing the nanodisc for all three structures were low pass filtered to 10 Å and scaled to a standard deviation of 1 (Chimera UCSF). All maps were aligned and resampled on the same grid and set to the same color. Images of 6.5 Å thick cross-section near the mid-point of the membrane (Extended Data Fig. 7d) at different σ thresholds was analyzed using ImageJ [51] (Extended Data Fig. 7a-c). In these images, a gray pixel denotes a point where the value of the density is above σ while a black one denotes a point where the density signal is below σ. The density of gray pixels in the map, $I(\sigma)$, was quantified near the pathways and dimer cavities (Extended Data Fig. 7a-c) at σ thresholds between 0.05 and 0.35, and normalized to the average gray pixel density of the whole nanodisc at the same σ value, $I_{nano}(\sigma)$. For $\sigma > 0.35$ the density of the whole membrane is too weak for quantification. The phenomenological parameter

$$I_N(\sigma) = \frac{I(\sigma)}{I_{nano}(\sigma)} \qquad (2)$$

reports how the density of the area considered varies relative to that of the whole nanodisc. Thus, $I_N(\sigma)<1$ indicates an area with relative weak density and conversely $I_N(\sigma)>1$ indicates an area of strong relative density. As positive control, a region of map corresponding to the protein was analyzed (TM10, Extended Data Fig. 7g). As expected $I_N(\sigma, TM10)$ increases with σ, as the protein density is higher than the membrane.

Gramicidin Fluorescence Assay

The gramicidin channel-based fluorescence assay for monitoring changes in lipid bilayer properties was implemented using large unilamellar vesicles (LUVs) incorporating gramicidin (gA) and loaded with 8-aminonaphthalene-1,3,6-trisulfonic acid, disodium salt (ANTS), following published protocols [27,52]. Vesicles composed of 1-palmitoyl-2-oleoyl-sn-glycero-3-phosphoethanolamine (POPE) and 1-palmitoyl-2-oleoyl-sn-glycero-3-phospho-1'-rac-glycerol (POPG) in 3:1 (mol/mol) proportion in chloroform were mixed with a gA to lipid molar ratio of 1:40,000. An additional 0, 1, or 5 mole-percent of C24 ceramide (d18:1/24:0) or C24:1 ceramide (d18:1/24:1) in chloroform were added to the gA-phospholipid mix. The lipid mixtures were dried under nitrogen to remove chloroform and further dried in vacuum overnight. Lipids were

bioRxiv preprint doi: https://doi.org/10.1101/420174; this version posted September 18, 2018. The copyright holder for this preprint (which was not certified by peer review) is the author/funder, who has granted bioRxiv a license to display the preprint in perpetuity. It is made available under aCC-BY-NC-ND 4.0 International license.

rehydrated with fluorophore-containing buffer solution (25 mM ANTS, 100 mM $NaNO_3$, and 10 mM HEPES), vortexed for 1 min, and incubated at room temperature for at least 3 hours while shielded from light. The solutions were sonicated for 1 min at low power and subjected to 6 freeze-thaw cycles. The samples then were extruded 21 times with an Avanti Polar Lipids mini-extruder (Avanti) and 0.1 mm polycarbonate filter. The samples were extruded at 35-40°C. Extravesicular ANTS was removed with PD-10 desalting column (GE Healthcare,) . The average LUV diameter was ~130 nm, with an average polydispersity index (PDI) of 10%, as determined using dynamic light scattering. LUV stock solutions were stored at room temperature with an average shelf life of 7 days.

The time course of the ANTS fluorescence was measured at 25 ^{o}C with an SX-20 stopped-flow spectrofluorometer (Applied Photophysics), with an LED light source. Excitation was at 352 nm and emission was recorded above 450 nm with a high pass filter; the deadtime of the instrument is ≈ 2 ms with a sampling rate of 5000 points/s. Samples were prepared by diluting the stock lipid concentration with buffer solution (140 mM NaOH and 10 mM HEPES) to 125 μM LUV; each sample was incubated for at least 10 min before several 1 s mixing reactions. Each sample was first mixed with the control buffer (no Tl^+), followed by mixing with the quench solution (50 mM $TlNO_3$ 94 mM $NaNO_3$ and 10 mM HEPES). Experiments are conducted with 2 independently prepared populations of vesicles per lipid/ceramide combination and traces are analyzed in MATLAB (MathWorks,).

The fluorescence quench rate therefore was determined as described [27] by fitting the time course to a stretched exponential function [53]:

$$F(t) = F(\infty) + \left[F(0) - F(\infty)\right] \cdot \exp\left[-\left(t/\mathrm{t}_0\right)^b\right] \tag{3}$$

$F(t)$ denotes the fluorescence intensities at time t; β ($0 < \beta \leq 1$) is a parameter that accounts for the dispersity of the vesicle population; and τ_o is a parameter with dimension of time. $F(0)$, $F(\infty)$, β and τ_o were determined from a nonlinear least squares fit of Eq. 1 to each individual fluorescence trace, and the quench rate was determined [53]:

$$Rate(t) = \frac{\beta}{\tau_0}\left[\frac{t}{\tau_0}\right]^{(\beta-1)} \tag{4}$$

evaluated at t = 2 ms. The ceramide-induced changes in the quench rate then was evaluated as

bioRxiv preprint doi: https://doi.org/10.1101/420174; this version posted September 18, 2018. The copyright holder for this preprint (which was not certified by peer review) is the author/funder, who has granted bioRxiv a license to display the preprint in perpetuity. It is made available under aCC-BY-NC-ND 4.0 International license.

$$Rate/Rate_{\text{cntrl}} = \frac{Rate(t)_{\text{ceramide}}}{Rate(t)_{\text{cntrl}}} \quad , \tag{5}$$

where the subscripts "ceramide" and "cntrl" denote the rates observed in the presence and absence of ceramide.

Data Availability

The three-dimensional cryo-EM density maps of the calcium-bound, calcium-free, and Ca^{2+}-bound in the presence of ceramide 24:0 afTMEM16/nanodisc complexes have been deposited in the Electron Microscopy Data Bank under accession numbers EMD-8948, EMD-8931, and EMDB-8959 respectively. The deposition includes corresponding masked and unmasked maps, the mask used for the final FSC calculation, and the FSC curves. Coordinates for the models of the calcium-bound, calcium-free, and Ca^{2+}-bound ceramide inhibited states have been deposited in the Protein Data Bank under accession numbers 6E0H, 6DZ7, and 6E1O respectively. All other data are available from the corresponding author upon reasonable request.

bioRxiv preprint doi: https://doi.org/10.1101/420174; this version posted September 18, 2018. The copyright holder for this preprint (which was not certified by peer review) is the author/funder, who has granted bioRxiv a license to display the preprint in perpetuity. It is made available under aCC-BY-NC-ND 4.0 International license.

References

1 Pomorski, T. & Menon, A. K. Lipid flippases and their biological functions. *Cell Mol Life Sci* **63**, 2908-2921 (2006).

2 Nagata, S., Suzuki, J., Segawa, K. & Fujii, T. Exposure of phosphatidylserine on the cell surface. *Cell Death Differ* **23**, 952-961, doi:10.1038/cdd.2016.7 (2016).

3 Falzone, M., Malvezzi, M., Lee, B. C. & Accardi, A. Known structures and unknown mechanisms of TMEM16 scramblases and channels. *JGP* **150**, 933-947, doi:doi: 10.1085/jgp.201711957 (2018).

4 Brunner, J. D., Lim, N. K., Schenck, S., Duerst, A. & Dutzler, R. X-ray structure of a calcium-activated TMEM16 lipid scramblase. *Nature* **516**, 207-212 (2014).

5 Jiang, T., Yu, K., Hartzell, H. C. & Tajkhorshid, E. Lipids and Ions Traverse the Membrane by the Same Physical Pathway in the. *eLife* **16**, 1-26, doi:10.7554/eLife.28671 (2017).

6 Yu, K. *et al.* Identification of a lipid scrambling domain in ANO6/TMEM16F. *eLife* **4**, 1-23, doi:10.7554/eLife.06901 (2015).

7 Lee, B. C. *et al.* Gating mechanism of the lipid pathway in a TMEM16 scramblase. *Nat Commun* (2018).

8 Bethel, N. P. & Grabe, M. Atomistic insight into lipid translocation by a TMEM16 scramblase. *Proc Natl Acad Sci USA* **113**, 14049-14054 (2016).

9 Dang, S. *et al.* Cryo-EM structures of the TMEM16A calcium-activated chloride channel. *Nature*, doi:10.1038/nature25024 (2017).

10 Paulino, C., Kalienkova, V., Lam, A. K. M., Neldner, Y. & Dutzler, R. Activation mechanism of the calcium-activated chloride channel TMEM16A revealed by cryo-EM. *Nature* **552**, 421-425, doi:10.1038/nature24652 (2017).

11 Lee, B.-C., Menon, Anant K. & Accardi, A. The nhTMEM16 Scramblase Is Also a Nonselective Ion Channel. *Biophysical Journal* **111**, 1919-1924, doi:10.1016/j.bpj.2016.09.032 (2016).

12 Malvezzi, M. *et al.* Out of the groove transport of lipids by TMEM16 and GPCR scramblases *PNAS*, doi:https://doi.org/10.1073/pnas.1806721115 (2018).

13 Peters, C. J. *et al.* The Sixth Transmembrane Segment Is a Major Gating Component of the TMEM16A Calcium-Activated Chloride Channel. *Neuron* **97**, 1063-1077.e1064, doi:https://doi.org/10.1016/j.neuron.2018.01.048 (2018).

14 Paulino, C. *et al.* Structural basis for anion conduction in the calcium-activated chloride channel TMEM16A. *eLife* **6**, 1-23, doi:10.7554/eLife.26232 (2017).

bioRxiv preprint doi: https://doi.org/10.1101/420174; this version posted September 18, 2018. The copyright holder for this preprint (which was not certified by peer review) is the author/funder, who has granted bioRxiv a license to display the preprint in perpetuity. It is made available under aCC-BY-NC-ND 4.0 International license.

15 Lim, N. K., Lam, A. K. M. & Dutzler, R. Independent activation of ion conduction pores in the double-barreled calcium-activated chloride channel TMEM16A. *JGP* **148**, 375-392, doi:10.1085/jgp.201611650 (2016).

16 Tien, J. *et al.* A comprehensive search for calcium binding sites critical for TMEM16A calcium-activated chloride channel activity. *Elife*, e02772, doi:10.7554/eLife.02772 (2014).

17 Terashima, H., Picollo, A. & Accardi, A. Purified TMEM16A is sufficient to form Ca2+-activated Cl- channels. *Proc Natl Acad Sci U S A* **110**, 19354-19359, doi:10.1073/pnas.1312014110 (2013).

18 Malvezzi, M. *et al.* Ca2+-dependent phospholipid scrambling by a reconstituted TMEM16 ion channel. *Nature Communications* **10.1038/ncomms3367** (2013).

19 Yu, K., Duran, C., Qu, Z., Cui, Y.-Y. & Hartzell, H. C. Explaining Calcium-Dependent Gating of Anoctamin-1 Chloride Channels Requires a Revised Topology. *Circulation Research* **110**, 990-999, doi:10.1161/CIRCRESAHA.112.264440 (2012).

20 O'Connell, A., Koeppe, R. & Andersen, O. Kinetics of gramicidin channel formation in lipid bilayers: transmembrane monomer association. *Science* **250**, 1256-1259, doi:10.1126/science.1700867 (1990).

21 Lewis, B. A. & Engelman, D. M. Lipid bilayer thickness varies linearly with acyl chain length in fluid phosphatidylcholine vesicles. *Journal of Molecular Biology* **166**, 211-217, doi:https://doi.org/10.1016/S0022-2836(83)80007-2 (1983).

22 Borodzicz, S., Czarzasta, K., Kuch, M. & Cudnoch-Jedrzejewska, A. Sphingolipids in cardiovascular diseases and metabolic disorders. *Lipids Health Dis* **14**, 55, doi:10.1186/s12944-015-0053-y (2015).

23 Hannun, Y. A. & Obeid, L. M. Principles of bioactive lipid signalling: lessons from sphingolipids. *Nat Rev Mol Cell Biol* **9**, 139-150, doi:10.1038/nrm2329 (2008).

24 Cantalupo, A. & Di Lorenzo, A. S1P Signaling and De Novo Biosynthesis in Blood Pressure Homeostasis. *J Pharmacol Exp Ther* **358**, 359-370, doi:10.1124/jpet.116.233205 (2016).

25 Deguchi, H., Yegneswaran, S. & Griffin, J. H. Sphingolipids as Bioactive Regulators of Thrombin Generation. *Journal of Biological Chemistry* **279**, 12036-12042, doi:10.1074/jbc.M302531200 (2004).

26 Hiroshi, D., J., E. D. & H., G. J. Minor plasma lipids modulate clotting factor activities and may affect thrombosis risk. *Research and Practice in Thrombosis and Haemostasis* **1**, 93-102, doi:doi:10.1002/rth2.12017 (2017).

27 Ingólfsson, H. I. & Andersen, O. S. Screening for Small Molecules' Bilayer-Modifying Potential Using a Gramicidin-Based Fluorescence Assay. *ASSAY and Drug Development Technologies* **8**, 427-436, doi:10.1089/adt.2009.0250 (2010).

bioRxiv preprint doi: https://doi.org/10.1101/420174; this version posted September 18, 2018. The copyright holder for this preprint (which was not certified by peer review) is the author/funder, who has granted bioRxiv a license to display the preprint in perpetuity. It is made available under aCC-BY-NC-ND 4.0 International license.

28 Andersen, O. S., Bruno, M. J., Sun, H. & Koeppe, R. E. in *Methods in Membrane Lipids* (ed Alex M. Dopico) 543-570 (Humana Press, 2007).

29 Lundbæk, J. A., Collingwood, S. A., Ingólfsson, H. I., Kapoor, R. & Andersen, O. S. Lipid bilayer regulation of membrane protein function: gramicidin channels as molecular force probes. *Journal of The Royal Society Interface* **7**, 373-395, doi:10.1098/rsif.2009.0443 (2010).

30 Alonso, A. & Goñi, F. M. The Physical Properties of Ceramides in Membranes. *Annual Review of Biophysics* **47**, 633-654, doi:10.1146/annurev-biophys-070317-033309 (2018).

31 García-Arribas, A. B. *et al.* Complex Effects of 24:1 Sphingolipids in Membranes Containing Dioleoylphosphatidylcholine and Cholesterol. *Langmuir* **33**, 5545-5554, doi:10.1021/acs.langmuir.7b00162 (2017).

32 Pinto, S. N., Silva, L. C., de Almeida, R. F. M. & Prieto, M. Membrane Domain Formation, Interdigitation, and Morphological Alterations Induced by the Very Long Chain Asymmetric C24:1 Ceramide. *Biophysical Journal* **95**, 2867-2879, doi:https://doi.org/10.1529/biophysj.108.129858 (2008).

33 Bruckner, R. J., Mansy, S. S., Ricardo, A., Mahadevan, L. & Szostak, J. W. Flip-Flop-Induced Relaxation of Bending Energy: Implications for Membrane Remodeling. *Biophysical Journal* **97**, 3113-3122, doi:https://doi.org/10.1016/j.bpj.2009.09.025 (2009).

34 Bennett, W. F. D., MacCallum, J. L. & Tieleman, D. P. Thermodynamic Analysis of the Effect of Cholesterol on Dipalmitoylphosphatidylcholine Lipid Membranes. *Journal of the American Chemical Society* **131**, 1972-1978, doi:10.1021/ja808541r (2009).

35 Sapay, N., Bennett, W. F. D. & Tieleman, D. P. Thermodynamics of flip-flop and desorption for a systematic series of phosphatidylcholine lipids. *Soft Matter* **5**, 3295-3302, doi:10.1039/B902376C (2009).

36 Drew, D. *et al.* GFP-based optimization scheme for the overexpression and purification of eukaryotic membrane proteins in Saccharomyces cerevisiae. . *Nat Protocols* **3**, 784-798 (2008).

37 Ritchie, T. K. *et al.* in *Methods in Enzymology* (Elsevier Masson SAS, 2009).

38 Suloway, C. *et al.* Automated molecular microscopy: The new Leginon system. *Journal of Structural Biology* **151**, 41-60, doi:https://doi.org/10.1016/j.jsb.2005.03.010 (2005).

39 Zheng, S. Q. *et al.* MotionCor2: anisotropic correction of beam-induced motion for improved cryo-electron microscopy. *Nature Methods* **14**, 331, doi:10.1038/nmeth.4193

https://www.nature.com/articles/nmeth.4193#supplementary-information (2017).

40 Rohou, A. & Grigorieff, N. CTFFIND4: Fast and accurate defocus estimation from electron micrographs. *Journal of Structural Biology* **192**, 216-221, doi:https://doi.org/10.1016/j.jsb.2015.08.008 (2015).

bioRxiv preprint doi: https://doi.org/10.1101/420174; this version posted September 18, 2018. The copyright holder for this preprint (which was not certified by peer review) is the author/funder, who has granted bioRxiv a license to display the preprint in perpetuity. It is made available under aCC-BY-NC-ND 4.0 International license.

41 Kimanius, D., Forsberg, B. O., Scheres, S. H. W. & Lindahl, E. Accelerated cryo-EM structure determination with parallelisation using GPUs in RELION-2. *eLife* **5**, e18722, doi:10.7554/eLife.18722 (2016).

42 Punjani, A., Rubinstein, J. L., Fleet, D. J. & Brubaker, M. A. cryoSPARC: algorithms for rapid unsupervised cryo-EM structure determination. *Nature Methods* **14**, 290-296, doi:10.1038/nmeth.4169 (2017).

43 Heymann, J. B. Bsoft: Image and Molecular Processing in Electron Microscopy. *Journal of Structural Biology* **133**, 156-169, doi:https://doi.org/10.1006/jsbi.2001.4339 (2001).

44 Cardone, G., Heymann, J. B. & Steven, A. C. One number does not fit all: Mapping local variations in resolution in cryo-EM reconstructions. *Journal of Structural Biology* **184**, 226-236, doi:10.1016/j.jsb.2013.08.002 (2013).

45 Emsley, P., Lohkamp, B., Scott, W. G. & Cowtan, K. Features and development of Coot. *Acta Crystallographica Section D* **66**, 486-501, doi:doi:10.1107/S0907444910007493 (2010).

46 Adams, P. D. *et al.* PHENIX: a comprehensive Python-based system for macromolecular structure solution. *Acta Crystallogr D Biol Crystallogr.* **66**, 213-221 (2010).

47 Afonine, P. V., Headd, J. J., Terwilliger, T. C. & Adams, P. D. PHENIX News. *Computational Crystallography Newsletter* **4**, 43-44 (2013).

48 Chen, V. B. *et al.* MolProbity: All-atom structure validation for macromolecular crystallography. *Acta Crystallographica Section D: Biological Crystallography* **66**, 12-21, doi:10.1107/S0907444909042073 (2010).

49 Barad, B. A. *et al.* EMRinger: Side chain-directed model and map validation for 3D cryo-electron microscopy. *Nature Methods* **12**, 943-946, doi:10.1038/nmeth.3541 (2015).

50 Pettersen, E. F. *et al.* UCSF Chimera - A visualization system for exploratory research and analysis. *Journal of Computational Chemistry* **25**, 1605-1612, doi:10.1002/jcc.20084 (2004).

51 Schneider, C. A., Rasband, W. S. & Eliceiri, K. W. NIH Image to ImageJ: 25 years of image analysis. *Nature Methods* **9**, 671, doi:10.1038/nmeth.2089 (2012).

52 Ingólfsson, H. I., Koeppe, R. E. n. & Andersen, O. S. Effects of green tea catechins on gramicidin channel function and inferred changes in bilayer properties. . *FEBS Lett.* **585**, 3101-3105 (2011).

53 Berberan-Santos, M. N., Bodunov, E. N. & Valeur, B. Mathematical functions for the analysis of luminescence decays with underlying distributions 1. Kohlrausch decay function (stretched exponential). *Chemical Physics* **315**, 171-182, doi:https://doi.org/10.1016/j.chemphys.2005.04.006 (2005).

54 Smart, O. S., Neduvelil, J. G., Wang, X., Wallace, B. A. & Sansom, M. S. HOLE: a program for the analysis of the pore dimensions of ion channel structural models. *J Mol Graph* **14**, 354-360 (1996).

bioRxiv preprint doi: https://doi.org/10.1101/420174; this version posted September 18, 2018. The copyright holder for this preprint (which was not certified by peer review) is the author/funder, who has granted bioRxiv a license to display the preprint in perpetuity. It is made available under aCC-BY-NC-ND 4.0 International license.

Author contributions

M.E.F. and A.A. designed research; M.E.F., A.R. and E.E. performed cryo-electron microscopy data collection; M.E.F. and J.R. analyzed cryo-EM data; M.E.F. and B.-C.L. performed and analyzed TMEM16 scrambling experiments; A.D.L and L.S. assisted with ceramide experiments; O.S.A. and T.P. performed and analyzed gramicidin flux assays; M.E.F. and A.A. wrote the manuscript; M.E.F., C.M.N., O.S.A., J.R. and A.A. edited the manuscript.

Acknowledgements

The authors thank members of the Accardi lab for helpful discussions. Richard Hite for helpful suggestions on cryo-EM data processing, Christopher Miller and Simon Scheuring for insightful discussions on the work, Jeremy Dittman for insightful discussions and artistic contributions to the work and Eva Fortea Verdejo for help with sequence alignments and artistic contributions. This work was supported by NIH Grant R01GM106717 (to A.A.) and 1R01GM124451-02 (to C.M.N.), an Irma T. Hirschl/Monique Weill-Caulier Scholar Award (to A.A.), by the Basic Science Research Program through the National Research Foundation of Korea (N.R.F.) funded by the Ministry of Education, Science and Technology (grant 2013R1A6A3A03064407 to B.-C. L.). All EM data collection and screening was performed at the Simons Electron Microscopy Center and National Resource for Automated Molecular Microscopy located at the New York Structural Biology Center, supported by grants from the Simons Foundation (349247), NYSTAR, and the NIH National Institute of General Medical Sciences (GM103310) with additional support from Agouron Institute (F00316) and NIH S10 OD019994-01. Initial negative stain screening was performed at the Weill Cornell Microscopy and Image Analysis Core Facility, with the help of L. Cohen-Gould, and at the Rockefeller University Electron Microscopy Resource Center, with the help of Kunihiro Uryu and Devrim Acehan.

Supplementary Information

Supplementary Information is available.

bioRxiv preprint doi: https://doi.org/10.1101/420174; this version posted September 18, 2018. The copyright holder for this preprint (which was not certified by peer review) is the author/funder, who has granted bioRxiv a license to display the preprint in perpetuity. It is made available under aCC-BY-NC-ND 4.0 International license.

Figure Legends

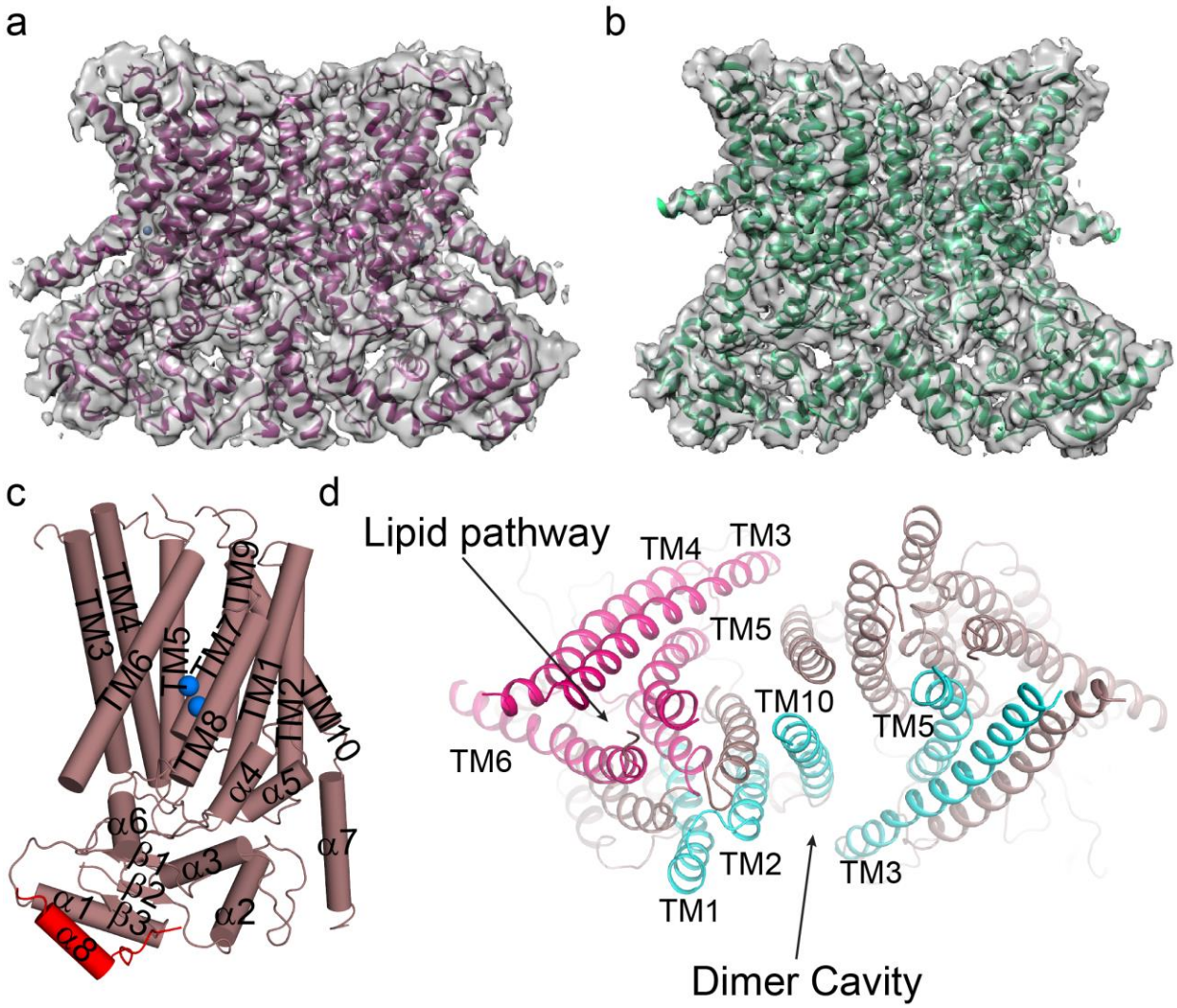

Figure 1: Structures of afTMEM16 in the presence and absence of Ca^{2+} a-b, Masked cryo-EM densities (gray transparent) used to build the atomic models of afTMEM16 reconstituted in nanodiscs in the presence of 0.5 mM Ca^{2+} (**a**) and in the absence of Ca^{2+} (**b**) with corresponding atomic models shown in cartoon representation. **c,** Helical organization of afTMEM16, the domain-swapped α8 from the other monomer is shown in red and Ca^{2+} ions are shown as blue spheres. **d**, Top view of Ca^{2+}-bound afTMEM16 highlighting the dimer cavity (cyan) and lipid translocation pathway (pink). Note that TM3 and TM5 are shared between the cavity and pathway.

bioRxiv preprint doi: https://doi.org/10.1101/420174; this version posted September 18, 2018. The copyright holder for this preprint (which was not certified by peer review) is the author/funder, who has granted bioRxiv a license to display the preprint in perpetuity. It is made available under aCC-BY-NC-ND 4.0 International license.

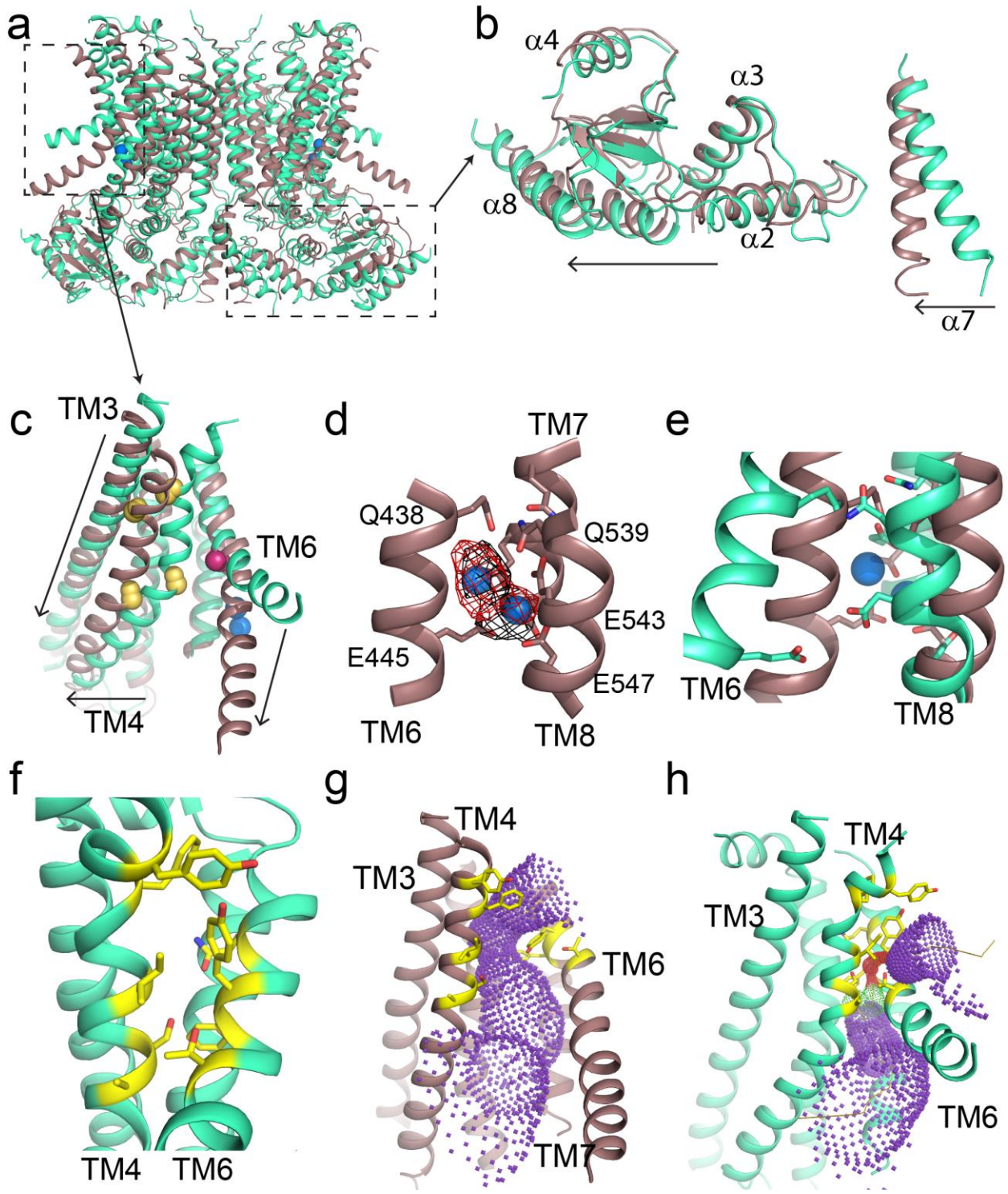

Figure 2 | Ca^{2+}-induced changes in afTMEM16: a, Structural alignment of afTMEM16 in the presence of 0.5 mM Ca^{2+} (maroon) and absence of Ca^{2+} (cyan) (blue sphere). The color scheme is the same throughout the figure. **b-c,** Close up views of the cytosolic domains (**b**) or lipid pathway (**c**). Arrows indicate direction of movement from the Ca^{2+}-free to the Ca^{2+}-bound conformations.

bioRxiv preprint doi: https://doi.org/10.1101/420174; this version posted September 18, 2018. The copyright holder for this preprint (which was not certified by peer review) is the author/funder, who has granted bioRxiv a license to display the preprint in perpetuity. It is made available under aCC-BY-NC-ND 4.0 International license.

The lipid permeation pathway (**c**) is constricted by rearrangements of TM4 around P324 and P333 (yellow spheres) and TM6 at A437 (red sphere). **d,** Close up view of the Ca^{2+}-binding site, with key coordinating residues shown as sticks. The density corresponding to the Ca^{2+} ions (blue spheres) from the experimental map is shown in black and the density from the calculated omit difference map is shown in red. The peak density corresponding to the Ca^{2+} ions in the omit difference maps (red mesh) is σ=13 and 7. **e,** Structural alignment of the binding site with and without Ca^{2+}. **f,** Close up view of the pathway. Residues at the interface with the membrane are shown as yellow sticks. **g-h,** Accessibility of the lipid permeation pathway estimated using the program HOLE [54] in the presence (**g**) or absence (**h**) of Ca^{2+}. Purple denotes areas of diameter d>5.5 Å, yellow areas where 5.5 < d < 2.75 Å and red areas with d<2.75 Å.

bioRxiv preprint doi: https://doi.org/10.1101/420174; this version posted September 18, 2018. The copyright holder for this preprint (which was not certified by peer review) is the author/funder, who has granted bioRxiv a license to display the preprint in perpetuity. It is made available under aCC-BY-NC-ND 4.0 International license.

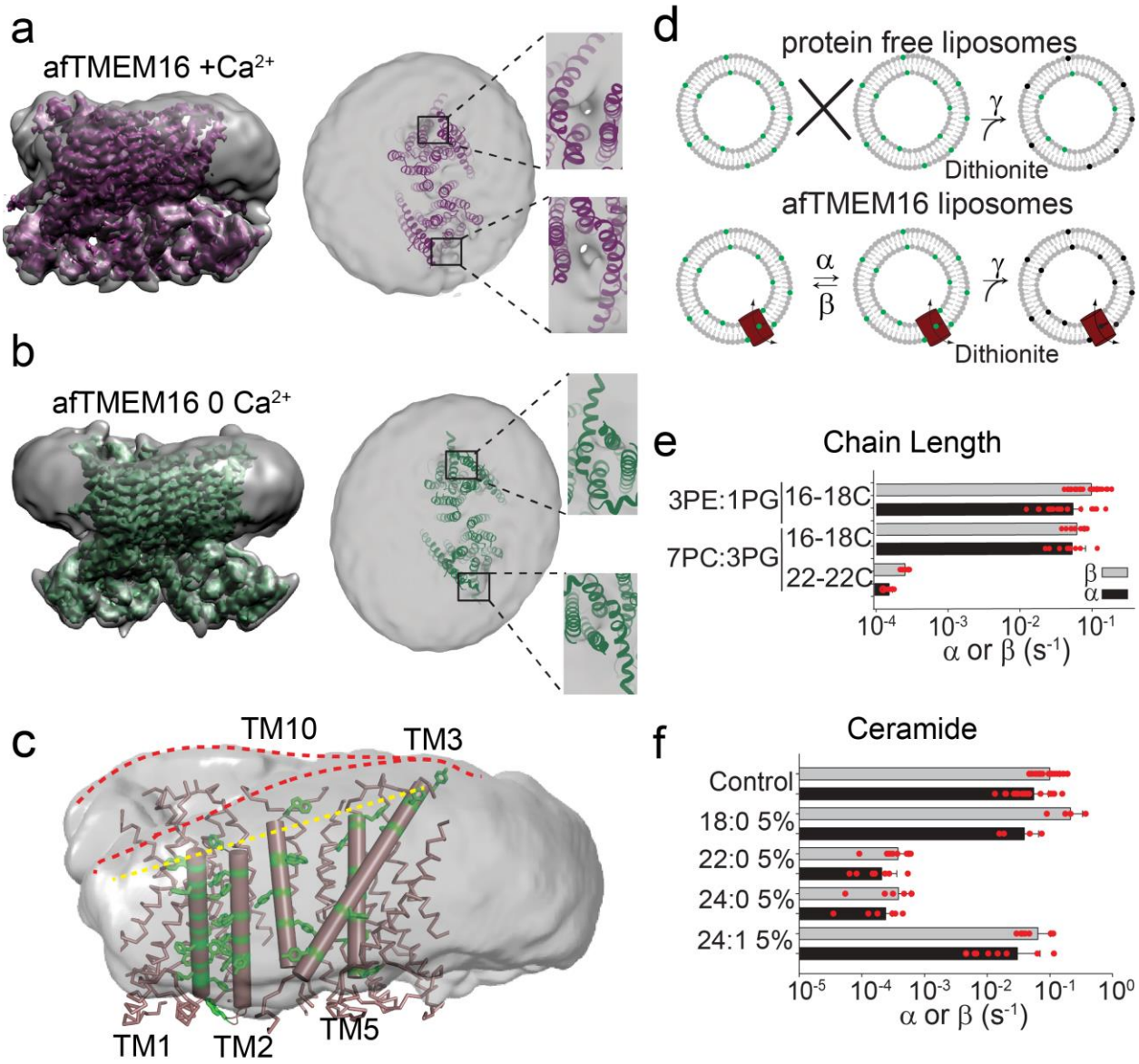

Figure 3 | Ca^{2+}-dependent membrane remodeling by afTMEM16 a-b, *Left panels*: masked maps of the afTMEM16/nanodisc complex with 0.5 mM Ca^{2+} (purple, **a**) and without Ca^{2+} (green, **b**) inside the respective unmasked map (gray) low pass filtered to 10 Å at σ=0.4. *Right panels*: top view of the unmasked map (grey) with (**a**) and without (**b**) Ca^{2+} low pass filtered to 10 Å at σ=0.1 with the respective atomic models shown as ribbons inside. Insets show close-up views of the densities at the permeation pathways. **c,** Bending of the outer leaflet at the dimer cavity in the presence of 0.5 mM Ca^{2+}. The low-pass filtered map of the complex was segmented and the

bioRxiv preprint doi: https://doi.org/10.1101/420174; this version posted September 18, 2018. The copyright holder for this preprint (which was not certified by peer review) is the author/funder, who has granted bioRxiv a license to display the preprint in perpetuity. It is made available under aCC-BY-NC-ND 4.0 International license.

isolated nanodisc density is shown. The afTMEM16 transmembrane region is shown in ribbon with the helices lining the dimer cavity (TM1, 2, 3, 5, and 10) in cartoon representation. Aromatic residues are shown as green sticks. Red dashed lines trace the upper membrane leaflet at the two sides of the lipid permeation pathway highlighting the opposite slant. Yellow dashed line traces the slope of the helices lining the dimer cavity. **d,** Schematic of the *in vitro* scramblase assay. Liposomes are reconstituted with NBD-labeled phospholipids (green) that distribute equally in the two leaflets. Addition of extraliposomal sodium dithionite reduces the NBD fluorophore (black), causing 50% fluorescence loss in protein free vesicles (top panel). When a scramblase is present (bottom panel), all NBD-phospholipids become exposed to dithionite, resulting in complete loss of fluorescence [18]. **e-f,** Forward (α, black) and reverse (β, grey) scrambling rate constants of afTMEM16 in 0.5 mM Ca^{2+} as a function of lipid chain length (**e**) or addition of 5 mole% of different ceramides (**f**). Rate constants were determined by fitting the fluorescence decay time course to Eq. 1. A 3 POPE: 1 POPG mixture was used for the reconstitutions containing ceramide lipids (**f**). For the chain length experiments liposomes were formed from a 7 POPC: 3 POPG mixture, which does not affect the scrambling rate constants (**e**). Data is reported as mean ± St.Dev. Red circles denote individual experiments. Values and exact repeat numbers are reported in Extended Data Table 2 and 3.

bioRxiv preprint doi: https://doi.org/10.1101/420174; this version posted September 18, 2018. The copyright holder for this preprint (which was not certified by peer review) is the author/funder, who has granted bioRxiv a license to display the preprint in perpetuity. It is made available under aCC-BY-NC-ND 4.0 International license.

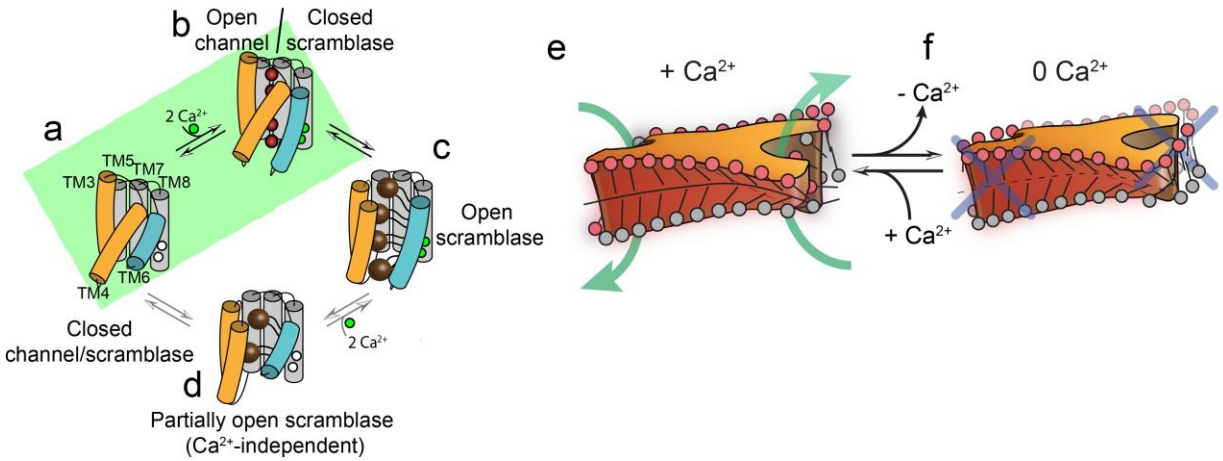

Figure 4 | Proposed mechanisms for gating and membrane remodeling by TMEM16 scramblases. a-d, Ca^{2+}-dependent gating scheme for TMEM16 scramblases. The α helices lining the lipid pathway and Ca^{2+}-binding site (TM3-8) are shown as cylinders. The two gating elements (TM3-4 and TM6) are respectively colored in orange and blue. When the Ca^{2+} binding sites are empty TM4 and TM6 are bent and occlude the pathway, resulting in a closed scramblase (PDBID: 6DZ7) (**a**). Upon Ca^{2+} binding, TM6 straightens and partly disengages from TM4, giving rise to a pathway that is closed to lipids but that can potentially allow ion permeation (a mTMEM16A-like state, PDBID:5OYG) (**b**). Rearrangement of TM6 promotes the straightening of TM4, resulting in an open lipid pathway (PDBID: 4WIS, 6E0H) (**c**). Straightening of TM4 in the absence of Ca^{2+}, would give rise to a partially open lipid pathway that might allow the experimentally observed Ca^{2+}-independent lipid scrambling [18] (**d**). If the straightening of TM4 is energetically unfavorable, the scramblase is restricted to visiting only states (**a**) and (**b**), green shaded area. This would give rise to the observed Ca^{2+}-dependent gating behavior of the TMEM16 channels. **e-f,** proposed mechanism for membrane remodeling by the afTMEM16 dimer. The architecture of the dimer cavity primes the membrane by bending it in opposite directions on the two sides of the lipid translocation pathway. In the presence of Ca^{2+} the pathway is open, enabling the formation of a membrane area that is thin and forming a conduit through which lipid headgroups can translocate between the two leaflets (**e**). In the absence of Ca^{2+} the pathway is closed preventing lipid scrambling (**f**).